

FEMTOLENSING: BEYOND THE SEMICLASSICAL APPROXIMATION

ANDREW ULMER¹ AND JEREMY GOODMAN²

Princeton University Observatory, Peyton Hall, Princeton, NJ 08544

Received 1994 June 6; accepted 1994 September 27

ABSTRACT

Femtolensing is a gravitational lensing effect in which the magnification is a function not only of the positions and sizes of the source and lens, but also of the wavelength of light. Femtolensing is the only known effect of $(10^{-13}–10^{-16} M_{\odot})$ dark-matter objects and may possibly be detectable in cosmological gamma-ray burst spectra. We present a new and efficient algorithm for femtolensing calculations in general potentials. The physical optics results presented here differ at low frequencies from the semiclassical approximation, in which the flux is attributed to a finite number of mutually coherent images. At higher frequencies, our results agree well with the semiclassical predictions. Applying our method to a point-mass lens with external shear, we find complex events that have structure at both large and small spectral resolution. In this way, we show that femtolensing may be observable for lenses up to $10^{-11} M_{\odot}$, much larger than previously believed. Additionally, we discuss the possibility of a search for femtolensing of white dwarfs in the Large Magellanic Cloud at optical wavelengths.

Subject headings: dark matter — gamma rays: bursts — gravitational lensing — methods: numerical

1. INTRODUCTION

The possibility of interference effects in gravitational lensing has been considered by several authors (Mandzhos 1981; Ohanian 1983; Schneider & Schmidt-Burgk 1985; Deguchi & Watson 1986; Peterson & Falk 1991; Gould 1992; Stanek, Paczyński, & Goodman 1993, hereafter SPG). Of particular interest are diffractive variations in flux with frequency ν when the source, lens, and observer occupy fixed positions. If the difference in time delay between a pair of images satisfies $\nu\Delta t \gg 1$, the fringe spacing is $\Delta\nu \approx \Delta t^{-1} \ll \nu$. We may call $\nu\Delta t \gg 1$ the “semiclassical” regime, because diffractive phenomena are produced by mutually coherent images whose positions, magnifications, and time delays can be determined using geometric optics. On the other hand, if $\nu\Delta t \lesssim 1$, regions of the lens plane other than the geometric optics images contribute importantly to the flux. The semiclassical approach then breaks down, and one must use the methods of physical optics.

If observed, interference effects would reveal dark-matter objects in a mass range to which few other tests are sensitive. The characteristic time delay produced by a lens of mass M is

$$\Delta t(M) = 2GM/c^3 = R_{\text{Sch}}/c, \quad (1)$$

where R_{Sch} is the Schwarzschild radius. Hence the condition $\nu\Delta t \sim 1$ is equivalent to $\lambda \sim R_{\text{Sch}}$. Since the Schwarzschild radius of the Sun is ≈ 3 km, broadband fringes ($\Delta\nu \sim \nu$) require decidedly substellar but nevertheless macroscopic lensing objects. In particular, Gould (1992) has shown that lens masses $M \sim 10^{-16}–10^{-13} M_{\odot} \sim 10^{17}–10^{20}$ g could produce observable fringes in gamma-ray burst (GRB) spectra at energies $E \sim 1$ MeV ($\lambda \sim 10^{-10}$ cm). Because the angular separation of the images produced by such a lens is $\sim 10^{-15}$ arcsec, Gould has coined the name “femtolensing” for this phenomenon. On the other hand, the probability that a randomly placed and cosmologically distant pointlike source should be lensed is $\sim \Omega_{\text{lens}}$, where the latter is the mean mass density in lensing objects

expressed as a fraction of the critical density $3H_0^2/8\pi G$ (Press & Gunn 1973). Given that $\sim 10^3$ GRBs have been detected to date (*Compton Gamma Ray Observatory* Sci. Rep. 1994), a single well-established case of femtolensing would indicate that objects $\sim 10^{-16} M_{\odot}$ contribute significantly to the mass density of the universe.

Even if copious lenses exist in the appropriate mass range, visible fringes can be seen only if the (incoherent) source is smaller than the Fresnel length $(\lambda D)^{1/2}$, where D is the distance. For source redshifts of order unity, this translates to $R_{\text{source}} \leq 10^{14} \lambda_{\text{cm}}^{1/2}$ cm. An additional constraint requires that, in order to have significant magnification, the source size must be smaller than the Einstein ring radius. For cosmological distances, $R_{\text{source}} \leq 5 \times 10^8 M/(10^{-16} M_{\odot})$ cm.

The rapid time variability of GRBs of 0.2 ms (Bhat et al. 1992) as well as the cosmological distances of ~ 0.5 Gpc for bright BATSE bursts found from $\log N$ – $\log P$ studies (Fenimore et al. 1993) suggest, however, that GRBs are sufficiently compact. There has been some confusion as to whether the appropriate linear source size should be taken from $\gamma c\Delta t$ or γct , where γ is the bulk Lorentz factor, c is the speed of light, Δt is the smallest variability timescale detected, and t is the total event duration. For many proposed cosmological scenarios, the appropriate measure is $\gamma c\Delta t$, because the last-scattering surface remains at approximately the same radius even though the relativistic ejecta may reach quite large distances in the course of the burst. For γ 's of 100–300 (e.g., Fenimore, Epstein, & Ho 1991), the (linear) size of a GRB last-scattering surface is of order 5×10^8 cm. Other models predict emission from patches on a relativistically expanding shell which can become extremely large (γct). In the latter case, it would be difficult to observe femtolensing because the interference patterns would differ from patch to patch. An observation of femtolensing could distinguish between the two scenarios.

SPG have discussed the possibility that line features in burst spectra may have been produced by femtolensing. Such lines have been seen or inferred in *Ginga* data (Murakami et al. 1988; Fenimore et al. 1988) and *Konus* data (Mazets et al. 1981) and have been attributed to cyclotron absorption. Like

¹ andrew@astro.princeton.edu.

² jeremy@astro.princeton.edu.

cyclotron lines, interference fringes would be evenly spaced in photon energy, and finite source size effects would create a decreasing amplitude for higher order fringes. No convincing evidence for lines has yet been seen in the largest homogeneous data set available, the BATSE experiment on the *Compton Gamma Ray Observatory*, although its capability of line detection is lower (Teegarden et al. 1993).

The femtolensing calculations cited above have considered only the simplest possible case, which is an isolated point-mass lens. The simplicity and symmetry of such a lens allow the physical optics problem to be solved in terms of known functions (Deguchi & Watson 1986). In the present paper, we present an efficient physical optics method for computing frequency-space fringes produced by general lenses. We assume that the lensing mass distribution is confined to a layer thin compared to the observer-source distance (single-screen approximation). We also neglect time dependence of the lensing geometry, which is permissible if the time-delay difference between any pair of images changes by less than ν^{-1} during an observation. The latter assumption is probably justified for femtolensing of GRBs (Gould 1992).

For definiteness, and because it is the simplest lens not yet treated in physical optics, we apply our methods to a single point mass with external shear. The computational approach taken, however, would apply equally well to an arbitrary surface density of lensing mass. Computational savings are achieved mainly by taking advantage of the achromaticity of gravitational lensing: that is, the time delays and excess optical path lengths are independent of frequency.

The plan of our paper is as follows. The physical optics problem is posed in § 2. We show how the scalar diffraction amplitude at the observer can be determined as a function of frequency by first calculating its Fourier transform, which is a function of time delay. An efficient numerical procedure for finding the latter function is developed in terms of contour integrals on the lens plane. The role of the geometric optics images and the correspondence with the semiclassical approximation is explained. In § 3 we describe certain details of our numerical implementation of the method and show that in the case of an isolated-point-mass lens, our results are consistent with those already obtained by Deguchi & Watson (1986) and SPG for the isolated-point-mass lens. In § 4 we present results for the more complex case of a point mass with external shear, which can produce up to four images. Finally, § 5 briefly summarizes the main points of our approach and prospects for observing femtolensing.

2. FORMALISM

The quantity of interest for femtolensing is the observed magnification as a function of frequency of the lensed source relative to the intensity in absence of a lens. In scalar diffraction theory, for the case of a thin screen, this function can be written as complex square of the amplitude

$$\Psi(\omega) = C_\omega \int_{-\infty}^{\infty} \int_{-\infty}^{\infty} dx dy \exp(i\omega\tau), \quad (2)$$

where ω is the photon frequency; C_ω is a normalization to unit flux in the absence of a lens that varies slowly with ω ; x and y are coordinates in the lens plane; and τ is the time delay function (e.g., Blandford & Narayan 1986):

$$\tau(\mathbf{r}) = \frac{1+z_l}{c} \left[\frac{d_{os}}{2d_{ol}d_{ls}} (\mathbf{r} - \mathbf{r}_s)^2 - \frac{2G}{c^2} \int dx' dy' \Sigma(\mathbf{r}') \ln |\mathbf{r} - \mathbf{r}'| \right]. \quad (3)$$

In the latter formula, z_l is the redshift of the lens; d_{os} , d_{ol} , and d_{ls} are angular diameter distances; $\mathbf{r}_s = (x_s, y_s)$ is the point where a direct line from observer to source would meet the lens plane in the absence of the lens; and $\Sigma(\mathbf{r})$ is the mass per unit area in the lens plane.

Although our methods are general, we illustrate them by application to a point mass with subcritical shear. If the observer and lens are on the z -axis and the source is slightly off-axis, the time-delay function for this case is, in normalized units (see Appendix A),

$$\tau(x, y, \mu, \phi, \theta) = (1 + \mu)x^2 + (1 - \mu)y^2 - 2\theta[x \cos(\phi) + y \sin(\phi)] - \ln(x^2 + y^2), \quad (4)$$

where μ is the shear, ϕ is the angle between the shear direction and that of the displacement of the source from the axis, and θ is the angle between the source and z -axis as measured by the observer in units of the angle subtended by the Einstein ring.

Direct calculation of $\Psi(\omega)$ is a three-dimensional problem in x , y , and ω . We demonstrate here a method to reduce the problem to two dimensions with use of Fourier transforms and contour integration. Dividing equation (2) by C_ω and taking the Fourier transform, we define

$$\tilde{\Psi}(t) \equiv \frac{1}{2\pi} \int_{-\infty}^{\infty} d\omega \exp(-i\omega t) \frac{\Psi(\omega)}{C_\omega}, \quad (5)$$

which can be viewed as a virtual pulse shape in time. After substitution from equation (2), this equation reduces to

$$\tilde{\Psi}(t) = \int_{-\infty}^{\infty} \int_{-\infty}^{\infty} dx dy \delta[\tau(x, y) - t]. \quad (6)$$

Therefore, the contribution to $\tilde{\Psi}(t)$ comes from curves of constant time delay; an example of such contours is shown in Figure 1.

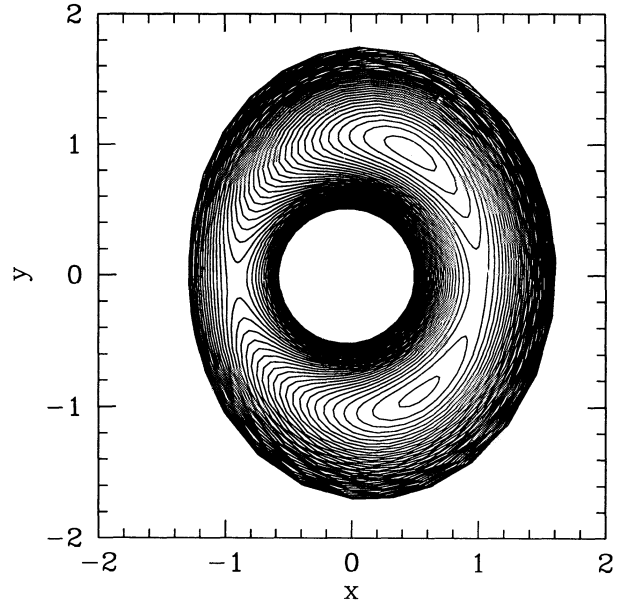


FIG. 1.—Contours of equal time delay in the image plane used to calculate $\tilde{\Psi}(t)$ (cf. Fig. 2). The empty circle in the middle contains the lens and therefore a logarithmic spike in time delay. Images form at critical points on this surface similar to those shown in Figs. 3c and 3d. Two minima form contours at low time delay on the top and bottom right of the depicted region. The contours merge at a saddle point on the right. This contour later splits to form inner and outer circular contours.

Equation (6) can be evaluated as a contour integral. Since $\tilde{\Psi}(t)dt$ is the area between the curves defined by $\tau(x, y) = t$ and $\tau(x, y) = t + dt$, and the distance between them is $dt/\|\nabla\tau\|$,

$$\tilde{\Psi}(t) = \oint \frac{ds}{\|\nabla\tau[x(s), y(s)]\|}, \quad (7)$$

where ds is the arc length along the curve defined below.

There will in general be more than one of these contours, though it is straightforward to find them all, as is described in the next section. The sum of the integrals (eq. [7]) over all contours $\{\gamma_k\}$ can be expressed as

$$\tilde{\Psi}(t) = \sum_k \left| \oint_{\gamma_k} du \right| \quad (8)$$

if the arc parameter u is defined through the differential equations

$$\frac{dx}{du} = -\frac{\partial\tau}{\partial y} \quad \text{and} \quad \frac{dy}{du} = \frac{\partial\tau}{\partial x}, \quad (9)$$

because

$$\frac{ds}{du} = \pm \sqrt{\left(\frac{\partial x}{\partial u}\right)^2 + \left(\frac{\partial y}{\partial u}\right)^2} = \pm \|\nabla\tau\|. \quad (10)$$

Notice that equations (9) are nonsingular near critical points if $\tau(\mathbf{r})$ is smooth.

We find $\tilde{\Psi}(t)$ is a smooth function except where t is equal to a critical value of the time-delay function so that $\|\nabla\tau\| = 0$ [an example of $\tilde{\Psi}(t)$ is shown in Fig. 2]. It is at these critical-valued time delays that images form. These singularities are calculated

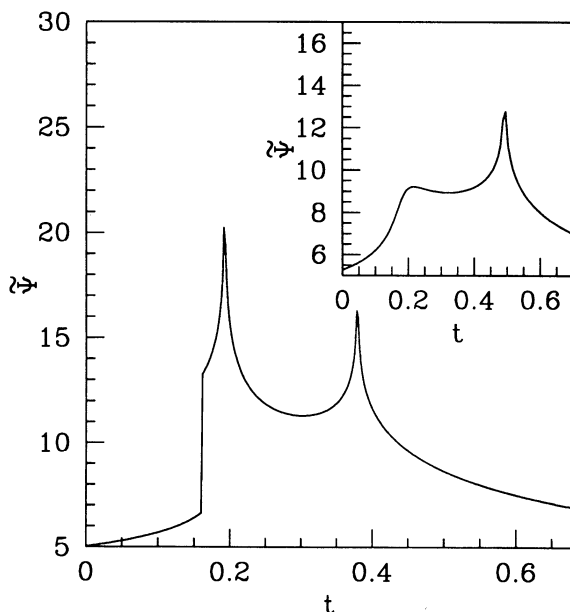


FIG. 2.— $\tilde{\Psi}(t)$, which yields the magnification amplitude, $\Psi(\omega)$, when Fourier-transformed. In this four-image geometry $\tilde{\Psi}(t)$ has four singularities (though the first occurs at minimum time delay). Two minima at low time delay cause discontinuities. Two saddle points at higher time delay contribute logarithmic spikes. The lens geometry resembles Figs. 3c and 3d. The inset shows $\tilde{\Psi}(t)$ in a case with only two images as the source approaches a caustic. The function resembles that of the four-image case. Whereas semiclassical results change discontinuously with the number of images, physical optics makes a smooth transition.

in Appendix B. For minima or maxima, there is a discontinuity in $\tilde{\Psi}(t)$ at the critical time, t_i , of

$$\lim_{\epsilon \rightarrow 0^+} [\tilde{\Psi}(t_i + \epsilon) - \tilde{\Psi}(t_i - \epsilon)] = \pm 2\pi \left[\frac{\partial^2\tau}{\partial x^2} \frac{\partial^2\tau}{\partial y^2} - \left(\frac{\partial^2\tau}{\partial x \partial y} \right)^2 \right]^{-1/2}. \quad (11)$$

In the case of a saddle point, $\tilde{\Psi}(t)$ diverges logarithmically near t_i , so that

$$\tilde{\Psi}(t) = -2 \ln |t - t_i| \left[\left(\frac{\partial^2\tau}{\partial x \partial y} \right)^2 - \frac{\partial^2\tau}{\partial x^2} \frac{\partial^2\tau}{\partial y^2} \right]^{-1/2} + \text{nonsingular part}. \quad (12)$$

Using a procedure described in the next section, the singularities can be dealt with and the inverse Fourier transform can be calculated, yielding the amplitude

$$\Psi(\omega) = C_\omega \int_{-\infty}^{\infty} \exp(i\omega\tau) \tilde{\Psi}(t) dt. \quad (13)$$

3. NUMERICAL IMPLEMENTATION

Except in the simplest circumstances, the method of § 2 must be applied numerically. For a point mass with shear, our algorithm computes the femtolensed energy spectra in 10–20 s on a Sparc 10 with accuracy beyond the resolution of the figures in this paper. Finer resolution would be needed only in cases where the source is very near to a caustic and high-frequency points are extremely important. Computer code which implements the algorithm is available upon request. The computation may be considered in three parts: location of the images, line integration on constant time delay contours, and calculation of the inverse Fourier transform of $\tilde{\Psi}(t)$ to yield $\Psi(\omega)$.

In the case of a point-mass lens with shear, the location of the images can be found analytically, so there is essentially no computational burden. However, one could envision more complex applications, such as lensing in a dense field with many lenses and images, where it would be necessary to utilize some image-finding scheme. An efficient image-finding algorithm has already been developed for microlensing calculations (Witt 1993). We find that the line integration around contours defined in equations (7)–(10) is the most computationally demanding part of the program. We expect that the total computational expense of our method should grow linearly with the number of geometric optics images. The number of images, N_i , is typically proportional to the number of masses, N_m . However, the upper bound on N_i is $\approx N_m^2$ (Witt 1990).

The method by which the contours are found warrants a brief discussion. An example of these contours is shown, for example, in Figure 1. The algorithm starts with a contour very close to the minimum time delay critical point. From there, it moves to larger time delay contours by taking small steps perpendicular to the contour. This method works as long as the number or topology of the contours does not change, but this happens only at the images. In other words, the contours are altered only when moving from below the time delay of an image to above it. When the image is a minimum in the time-delay surface, a new contour is formed around the minimum. When the contour is a saddle point, a contour either splits into two, or two contours merge. One can distinguish between these cases by monitoring the line integral at contours near each time delay of an image. Maxima are not encountered if the lens consists solely of point masses and shear.

Using the line integrals, we determine $\tilde{\Psi}(t)$ for a range of values of τ . We take these values linearly spaced, though future versions of the algorithm could sample the function more efficiently. Uniform sampling allows us to use fast Fourier transform (FFT) methods to perform the discrete Fourier transform (DFT), but finding and integrating along the contours would have dominated the computation time even if we had performed the DFT by direct $O(N^2)$ methods. The computations for one geometry are shown in Figure 2. We find generally that one needs ~ 1000 points taken uniformly between the minimum time delay and the point at which $\tilde{\Psi}(t)$ reaches $\sim 1\%$ of its asymptotic value. It is impossible to reconstruct the entire detail of the $\tilde{\Psi}(t)$ curve with such measurements because, for instance, near the time delay of a saddle-point image there is a logarithmic divergence as discussed in the previous section and Appendix B. We account for this loss of detail near the critical time delays by subtracting the analytic forms of the singularities (eqs. [11] and [12]) and dealing with them separately:

$$\tilde{\Psi}'(t) = \sum_k \left| \oint_{\gamma_k} du \right| - \text{singular part} . \quad (14)$$

We then perform a DFT of $\tilde{\Psi}'(t)$ while paying close attention to edge effects. Finally, we calculate the exact Fourier transforms of the divergences and discontinuities and add them to the DFT to obtain $\Psi(\omega)$.

As a test of this procedure, the calculation is carried out in the simplified case of a point mass without shear and is shown in Figure 4 (*top panel*). This calculation agrees with an earlier calculation of the same result which utilized independent methods (SPG) to the resolution of the figures presented in this paper.

4. RESULTS

Using the new algorithm, we investigated the interference produced by a variety of lensing geometries for a point source and lens with shear (extended sources could be calculated by repeatedly applying the algorithm for source points chosen, e.g., by Gaussian quadrature weightings). Figures 4 and 5 show the results of calculations for various source/lens configurations depicted in Figure 3. The frequency, ω , is given in dimensionless units:

$$\text{frequency: } \omega \equiv \frac{\tilde{\omega}(1+z_L)R_{\text{Sch}}}{c} = \frac{2\pi(1+z_L)R_{\text{Sch}}}{\lambda} , \quad (15)$$

where R_{Sch} is the Schwarzschild radius and λ is the wavelength. For example, unity corresponds to photon energy of 1 keV and a mass of $\sim 5 \times 10^{-14} M_\odot$ at $z_L = 0.5$. A sinusoidal pattern is produced which has a frequency inversely proportional to the difference in time delay for the two images. The top panel of Figure 4 shows the interference pattern for a point mass with no shear for which the semiclassical approximation is an extremely good approximation.

Using our algorithm, external shear can be introduced into the calculation. We find that, when the source approaches the caustic, the physical optics calculation differs from the semiclassical approximation. For example, the bottom panel of Figure 4 shows a two-image interference pattern for which the first few interference nodes have largely different amplitudes. At high frequencies, the semiclassical approximation approaches the physical optics solution.

The interference patterns become much more complex when the source lies inside the center caustic region. There, four

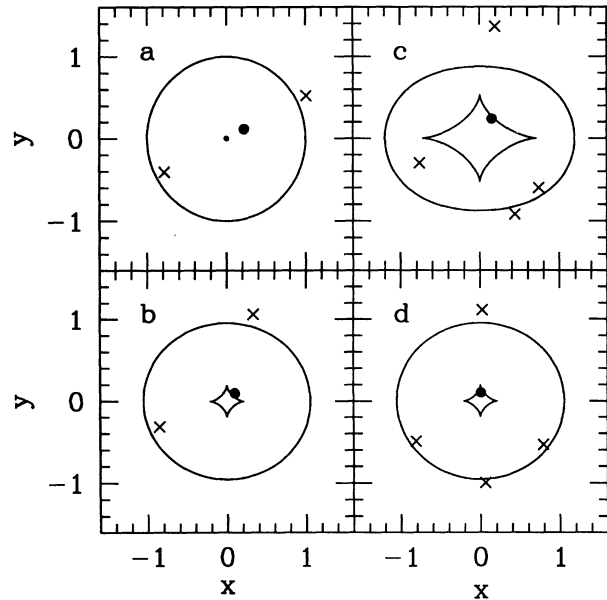


FIG. 3.—Image positions (crosses), critical curves (circle and ovals), projected source positions (large dots), projected caustics (small dot and diamonds) in dimensionless units for a variety of geometries. (a) Point mass without shear, so the caustic is the Einstein ring. (b)–(d) Shears of 0.1, 0.3, and 0.1, respectively.

images form, and the interference patterns become chaotic. Figure 5 shows the magnification as a function of frequency for two such cases. The main characteristics to note are that the interference patterns can become quite complex with oscillations with both long and short periods (the bottom panel shows both the physical optics magnification and a smoothed magnification). In short, this means that femtolensing can be observed over a wider range of frequency space and, therefore,

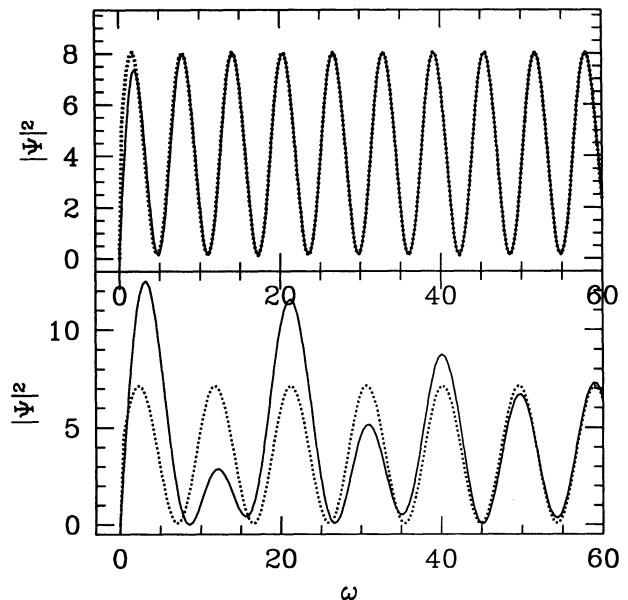


FIG. 4.— $|\Psi|^2$, the magnification as a function of dimensionless frequency for the geometries in Figs. 3a and 3b (*top and bottom*, respectively). Solid line: Physical optics calculation calculated with our algorithm. Dotted line: Semiclassical, or two-ray, approximation discussed in Appendix B. When the source approaches a caustic, the energy spectrum cannot be accurately calculated with the semiclassical approximation at lower frequencies.

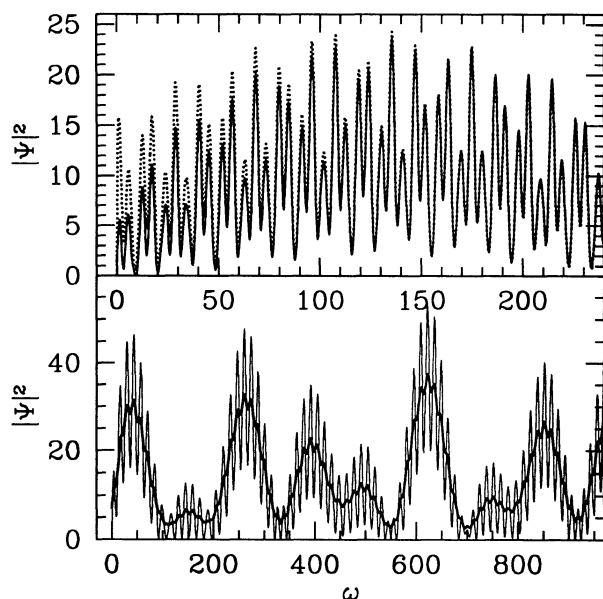


FIG. 5.—Magnification as a function of dimensionless frequency for the geometries in Figs. 3c and 3d (top and bottom, respectively). Complex beat frequencies are created between the time delays of the four images so that the semiclassical approximation (dotted line, top panel) is inaccurate. The beat frequencies create features on a much broader energy range as exemplified by the bottom panel in which a smoothed magnification curve is superposed on the physical optics calculation.

a wider range of masses than originally believed. Figure 5 shows that the typical interference patterns, corresponding to inverse time delays, can be hundreds of times larger than the characteristic time delay (see eq. [1]), so the lens masses can be hundreds of times larger than those discussed by Gould and SPG. The short-period interference, which has been discussed in previous papers, can be seen in the top panel of Figure 4. The long-period interference occurs when two of the four images have very close time delays, which is a common result with four images. Appendix C shows that in these circumstances the separation of the long-period fringes increases as the cube of the total magnification, and the source-size limit is somewhat more severe than the Fresnel length.

The complex nature of the magnification in Figure 5 can be understood to some extent in the semiclassical regime, because there one finds that the complex amplitude of magnification, $\Psi(\omega)$, is composed of a set of sinusoidal interference fringes from each pair of images. For four images, there are six pairs which each produce sinusoidal interference. The resulting interference pattern, which is the squared sum of these sine waves, will in general be very complex. The physical optics calculation is qualitatively similar, but yields different magnifications and different specific structures at low frequencies. According to the result (44) in Appendix C, the first few long-period fringes are least sensitive to the angular size of the source.

5. DISCUSSION

We find that even in the simplified case of a point mass with external shear, very complex interference patterns can be formed. In reality, however, the patterns should be even more

complex. In addition to external shear, one should account for local shear from neighbors for femtolensing matter in galactic halos. Complex, many-image geometries will result, and as found in the case of a point mass with external shear, images with smaller-than-characteristic difference in time delay (see eq. [1]) will cause surprisingly long period interference patterns (e.g., Fig. 5) which allow for detection of larger masses. For an external shear of 0.1, we expect these complex interference patterns to occur 3% of the time that a source is found inside the Einstein radius. In general, for a halo mass distribution similar to a singular isothermal sphere, the shear would have a scale length of 5 kpc, so that between 10 and 50 kpc, the shear would be 0.5–0.1, so these complex patterns would occur much more often. Furthermore, there would be a magnification bias (see Appendix C) toward these complex events, which could likely increase the observed fraction by an order of magnitude.

Cosmological GRBs are considered the best candidates to show femtolensing because of their extremely small angular size. If the line of sight to a GRB passed through a galaxy and if the dark halo mass is composed of $\sim 10^{-11}$ – $10^{-16} M_{\odot}$ (we increase the range of masses by a factor of 100 as a result of the long-period events discussed above), then one could expect to see, in addition to macro- or microlensing, femtolensing effects as well. The femtolensing could easily mimic other emission or absorption-line processes. We suggest, then, that, if a spectral absorption or emission feature is definitively observed in a GRB due to femtolensing, it is likely that the burst would be macrolensed as well. Additionally, macrolensing would produce multiple images (bursts) which would likely be femtolensed and therefore increase the number of expected femtolensed events.

Although the source-size requirements exclude the possibility of ever detecting femtolensing in main-sequence stars in nearby galaxies, in the future it may be possible to detect femtolensing of white dwarfs. (We are grateful to B. Paczyński for pointing this out.) In order for the fringes to have separation of 0.2 eV (a typical optical bandwidth), the lensing masses would be in the range $M \sim 10^{-9}$ – $10^{-11} M_{\odot}$ for short to characteristic time delays, respectively. In the Large Magellanic Cloud (LMC), the maximum magnification possible for such events as determined by the ratio of the Einstein ring to source size would be ~ 2 –20, where the larger masses cause the higher magnification. For a white-dwarf source in the LMC observed at 1 eV, the requirement that the source be smaller than the Fresnel length, $(\lambda D)^{1/2} = 3 \times 10^9$ is met ($D = D_{\text{LMC}}/2 = 25$ kpc). These events would be quite short (≤ 1 minute), due to relative velocities and a small Einstein ring, relative to current microlensing events (e.g., Paczyński 1986). However, it is not yet possible to monitor white dwarfs in the LMC, so one would have to adopt an observing strategy for transients—possibly in the ultraviolet—similar to that of supernovae searches. In contrast to current microlensing studies, detection techniques would be based on anticorrelation of the flux variation in different wavelength bands.

This work was supported in part by the David and Lucille Packard Foundation and NASA grant NAG 5-1901. It is a pleasure to acknowledge B. Paczyński for suggesting the white-dwarf lensing scenario, and E. E. Fenimore, R. Nityayanda, K. Z. Stanek, and H. Witt for discussions.

APPENDIX A

NORMALIZATIONS

In this Appendix, we describe the normalized units used in the formulae above. We begin with the time-delay formula for a point mass with shear (e.g., Blandford & Narayan 1992):

$$\tilde{\tau}(\tilde{x}, \tilde{y}, \tilde{\mu}, x_s, y_s) = \frac{1+z_l}{c} \left[\left(\frac{1}{2D} + \tilde{\mu} \right) \tilde{x}^2 + \left(\frac{1}{2D} - \tilde{\mu} \right) \tilde{y}^2 - \frac{(x_s \tilde{x} + y_s \tilde{y})}{d_{ls}} - R_{\text{Sch}} \ln(\tilde{x}^2 + \tilde{y}^2) \right], \quad (16)$$

where z_l is the lens redshift, \tilde{x} and \tilde{y} are points at which the ray intersects the lens plane, x_s and y_s give the location of the source in the source plane, R_{Sch} is the Schwarzschild radius, and $D = d_l d_{ls}/d_s$ where d_l , d_s , and d_{ls} are angular diameter distances. Throughout the derivation, additive constants in the time delay will be ignored.

The form for $\Psi(\omega)$ is

$$\Psi(\tilde{\omega}) = \tilde{C}_{\tilde{\omega}} \int_{-\infty}^{\infty} \int_{-\infty}^{\infty} d\tilde{x} d\tilde{y} \exp(i\tilde{\omega} \tilde{\tau}). \quad (17)$$

Then, we define the following dimensionless variables:

$$\text{time delay: } \tau \equiv \frac{\tilde{\tau}c}{(1+z_l)R_{\text{Sch}}}, \quad (18)$$

$$\text{frequency: } \omega \equiv \frac{\tilde{\omega}(1+z_l)R_{\text{Sch}}}{c} = \frac{2\pi(1+z_l)R_{\text{Sch}}}{\lambda}, \quad (19)$$

$$\text{position (image plane): } (x, y) \equiv \frac{(\tilde{x}, \tilde{y})}{\sqrt{2DR_{\text{Sch}}}}, \quad (20)$$

$$\text{shear: } \mu \equiv 2DR_{\text{Sch}}\tilde{\mu}, \quad 0 \leq \mu \leq 1. \quad (21)$$

With these definitions, equation (17) becomes equation (2), and C_{ω} , which normalizes the magnification to a unit flux, can then be shown to be

$$C_{\omega} = \frac{i\omega}{\pi}. \quad (22)$$

Equation (18) can be rewritten, after substituting the dimensionless variables, as

$$\tau(x, y, \mu, x_s, y_s) = (1+\mu)x^2 + (1-\mu)y^2 - \frac{\sqrt{2D}(x_s x + y_s y)}{d_{ls}\sqrt{R_{\text{Sch}}}} - \ln(x^2 + y^2). \quad (23)$$

Finally, we choose an impact parameter

$$\theta \equiv \frac{\sqrt{x_s^2 + y_s^2}}{d_s R_E}, \quad (24)$$

where R_E is the Einstein radius:

$$R_E \equiv \sqrt{\frac{2R_{\text{Sch}} d_{ls}}{d_l d_s}}. \quad (25)$$

We also pick ϕ so that we recover equation (4):

$$\tau(x, y, \mu, \phi, \theta) = (1+\mu)x^2 + (1-\mu)y^2 - 2\theta[x \cos(\phi) + y \sin(\phi)] - \ln(x^2 + y^2). \quad (26)$$

APPENDIX B

SEMICLASSICAL APPROXIMATION

Herein we discuss the behavior of $\tilde{\Psi}(t)$ near critical points (images), so that the divergent portions of the function can be subtracted to yield a smooth function that can be computationally sampled and transformed. When the frequency is larger than the minimum separation of image time delays, i.e., $\omega \gg |\tau_i - \tau_j|$ for all i, j , it is in the semiclassical region and these singularities dominate $\Psi(\omega)$. In any regime, the singular behavior dominates $\tilde{\Psi}(t)$ near the time delays of the images.

We consider the two cases of a minimum/maximum and a saddle point.

B1. MINIMUM/MAXIMUM

Near a critical point at the origin, a contour is given by

$$\tau = \pm \left(\frac{x^2}{2a^2} + \frac{y^2}{2b^2} \right) + t_{\text{crit}}, \quad (27)$$

where t_{crit} is the time delay at the critical point $x = y = 0$. Without loss of generality we consider the case of a minimum only. The contribution of the singularity to $\tilde{\Psi}(t)$ is found by the integral (see eqs. [1]–[14])

$$\left| \oint du \right|, \quad \text{where } \frac{dx}{du} = -\frac{\partial \tau}{\partial y}, \quad \frac{dy}{du} = \frac{\partial \tau}{\partial x}. \quad (28)$$

We write

$$\frac{d^2 x}{du^2} = -\left(\frac{d}{du} \right) \left(\frac{\partial \tau}{\partial y} \right) = -\left(\frac{d}{du} \right) \left(\frac{y}{b^2} \right) = -\frac{x}{a^2 b^2}, \quad (29)$$

so that

$$x = A \cos \left(\frac{u}{ab} + \phi \right) \quad (30)$$

and

$$\oint du = 2\pi ab. \quad (31)$$

Further, from equation (27),

$$\frac{1}{a^2 b^2} = \frac{\partial^2 \tau}{\partial x^2} \frac{\partial^2 \tau}{\partial y^2} - \left(\frac{\partial^2 \tau}{\partial x \partial y} \right)^2 \equiv \det H. \quad (32)$$

The singularity is such, therefore, that

$$\Delta \tilde{\Psi}(t) = \begin{cases} 0 & \text{if } t < t_{\text{min}}, \\ 2\pi/\sqrt{\det H} & \text{if } t > t_{\text{min}}. \end{cases} \quad (33)$$

This term can be removed from the slowly varying part of $\tilde{\Psi}(t)$ and Fourier-transformed to yield the semiclassical contribution as

$$\Delta \Psi(\omega) = C_\omega \int dt \exp(i\omega t) \Delta \tilde{\Psi} = \frac{-2 \exp(i\omega t_{\text{min}})}{\sqrt{\det H}}. \quad (34)$$

B2. SADDLE POINT

In a similar manner as above, the singularity of a saddle point may be calculated. Without loss of generality we consider this orientation of saddle point:

$$\tau = \left(\frac{x^2}{2a^2} - \frac{y^2}{2a^2} \right). \quad (35)$$

By analogy with the last derivation, we have

$$x = A \cosh(u/ab). \quad (36)$$

In this case the contours are hyperbolic rather than elliptical and do not close locally. To compute the contribution from the neighborhood of the critical point, we consider that part of each contour for which $|x| < x_0$, where x_0 is fixed as $\tau \rightarrow t_{\text{crit}}$. Finding u_0 such that $x(u_0) = x_0$ and taking $|u_0/ab| \gg 1$, we have

$$u_0 = ab \cosh^{-1} \left(\frac{u_0}{ab} \right) \rightarrow \frac{1}{2} ab \log \left(\frac{2x_0}{A} \right) = -\frac{1}{2} ab \log |t - t_{\text{crit}}| + \text{constant}, \quad (37)$$

where the constant depends on the choice of x_0 . The contour extends from $-u_0$ to u_0 on each of two branches of the hyperbola, so

$$\Delta \tilde{\Psi}(t) = -2ab \log |t - t_{\text{crit}}| = \frac{-2 \log |t - t_{\text{crit}}|}{\sqrt{-\det H}}. \quad (38)$$

When Fourier-transformed, $\Delta \tilde{\Psi}(t)$ yields the semiclassical contribution,

$$\Delta \Psi(\omega) = C_\omega \int dt \exp(i\omega t) \Delta \tilde{\Psi} = \frac{2i \exp(i\omega t_{\text{crit}})}{\sqrt{-\det H}}. \quad (39)$$

APPENDIX C

PHYSICAL OPTICS OF MERGING IMAGES

When the flux is dominated by two bright images near a critical line, the time-delay surface can be approximated locally by

$$\tau(x, y; x_s, y_s) = \frac{x^3}{3a^3} + \frac{y^2}{b^2} - x_s x - y_s y. \quad (40)$$

Here (x_s, y_s) is the undeflected source position in the lens plane. We use the dimensionless units of Appendix A, but the local coordinates in equation (40) are centered on the critical line ($x = 0$) rather than the deflecting mass. The parameters a and b are assumed to be ~ 1 , but their precise values depend on the global geometry of the time-delay surface.

Sufficiently near a caustic, diffraction phenomena are universal and independent of the details of the lens. Thus, results motivated by, for example, reflection of laser light from uneven surfaces can be carried over to femtolensing essentially without change. A very good review of the physical optics of caustics is Berry & Upstill (1980). Some aspects of diffraction by fold caustics, the main subject of this Appendix, have been discussed in the context of gravitational lensing by Ohanian (1983). Little of what follows is new, but we go over it here because of the special features of femtolensing—especially the fact that we are concerned with fringes in frequency rather than position.

For $x_s > 0$, geometric optics yields two images at $x = \pm a^{3/2} x_s^{1/2}$ with net flux

$$F_{\text{geo}}(x_s) = 2a^{3/2}b^2x_s^{-1/2}. \quad (41)$$

On the other hand, the amplitude (eq. [2]) can be evaluated directly:

$$F(x_s, \omega) = |\psi(\omega; x_s, y_s)|^2 = 4\pi\omega^{1/3}a^2b^2 |\text{Ai}(-ax_s\omega^{2/3})|^2. \quad (42)$$

The Airy function quickly approaches the asymptotic approximation (e.g., Abramowitz & Stegun 1972)

$$\text{Ai}(-\xi) \approx \pi^{-1/2}\xi^{-1/4} \sin\left(\frac{2}{3}\xi^{3/2} + \frac{\pi}{4}\right) \quad \text{if } \xi \geq 1, \quad (43)$$

so that the flux (eq. [42]) displays fringes with spacing

$$\Delta\omega_f = \frac{3\pi}{2} (ax_s)^{-3/2}; \quad (44)$$

in fact, even the position of first zero in the flux is accurately predicted by the asymptotic form (43), which is the semiclassical prediction. Both geometric optics and the semiclassical theory predict a divergent flux as $x_s \rightarrow 0$. But, since $\text{Ai}(0) = 3^{-2/3}/\Gamma(\frac{2}{3})$, the flux at the caustic is finite and scales as $\omega^{1/3}$.

Comparing equations (41) and (44), we see that *the fringe spacing scales as the cube of the total magnification*. This accounts for the long-period fringes that we often see in our numerical spectra. Because of magnification bias, observed fringes should typically be much more widely spaced than the naive scaling $\Delta\tilde{\omega} \sim c/R_{\text{Sch}}$ assumed in earlier work.

A source of finite angular size can be regarded as an ensemble of incoherent points. If fringes are to be visible, the phase of the Airy function in equation (42) must vary by less than the fringe spacing (eq. [44]) across the source. Therefore the angular size must satisfy

$$\theta_s \lesssim \theta_E \frac{0.6}{a} \left(\frac{\Delta\omega_f}{\omega}\right) \omega^{-2/3}, \quad (45)$$

where $\theta_E \equiv (2DR_{\text{Sch}})^{1/2}/d_l$ is the angular radius of the Einstein ring. For images close to a critical line, this limit supersedes the angular-size limit associated with the Fresnel length, which scales as $\omega^{-1/2}$. To achieve fringes of a given physical frequency $\tilde{\omega}$ and spacing $\Delta\tilde{\omega}$ with lenses whose Schwarzschild radius is much larger than the wavelength, the limit on the source size scales as $R_{\text{Sch}}^{-1/6}$.

The fringe visibility drops very rapidly as θ_s increases beyond the limit (eq. [45]). If the unlensed source intensity varies smoothly on the sky—as a Gaussian, for example, but not a uniform disk—then the fringe visibility damps exponentially with θ_s , and as predicted by equation (45), the higher fringes damp more rapidly than the first one.

Given a sufficiently compact source, the highest amplifications occur near a cusp, as in Figure 3d. The cusp produces up to three bright images of a point source. The time-delay function must be approximated by a polynomial of at least fourth degree, instead of the cubic (eq. [40]) that describes a simple fold caustic. Diffraction by cusps has been analyzed by Pearcey (1946) and reviewed by Berry & Upstill (1980).

REFERENCES

- | | |
|--|--|
| <p>Abramowitz, M., & Stegun, I. A. 1972, <i>Handbook of Mathematical Functions</i> (Washington, DC: GPO)</p> <p>Berry, M. V., & Upstill, C. 1980, <i>Prog. Optics</i>, 18, 257</p> <p>Bhat, P. N., Fishman, G. J., Meegan, C. A., Wilson, R. B., Brock, M. N., & Paciesas, W. S. 1992, <i>Nature</i>, 359, 217</p> <p>Blandford, R. D., & Narayan, R. 1986, <i>ApJ</i>, 310, 568</p> <p>———. 1992, <i>ARA&A</i>, 30, 311</p> | <p><i>Compton Gamma Ray Observatory Sci. Rep.</i> 1994, 157 (electronic)</p> <p>Deguchi, S., & Watson, W. D. 1986, <i>ApJ</i>, 307, 30</p> <p>Fenimore, E. E., et al. 1988, <i>ApJ</i>, 335, L71</p> <p>———. 1993, <i>Nature</i>, 366, 40</p> <p>Fenimore, E. E., Epstein, R. I., & Ho, C. 1993, <i>A&AS</i>, 97, 59</p> <p>Gould, A. 1992, <i>ApJ</i>, 386, L5</p> <p>Mandzhos, A. V. 1981, <i>Soviet Astron. Lett.</i>, 7, 213</p> |
|--|--|

- Mazets, E. P., Golenskii, S. V., Aptekar, R. L., Guryan, Y. A., & Ilyinskii, V. N.
1981, *Nature*, 290, 378
Murakami, T., et al. 1988, *Nature*, 335, 234
Ohanian, H. C. 1983, *ApJ*, 271, 551
Paczynski, B. 1986, *ApJ*, 304, 1
Pearcey, T. 1946, *Phil. Mag.*, 37, 311
Peterson, J. B., & Falk, T. 1991, *ApJ*, 374, L5
Press, W. H., & Gunn, J. E. 1973, *ApJ*, 185, 397
Schneider, P., & Schmidt-Burgk, J. 1985, *A&A*, 148, 369
Stanek, K. Z., Paczynski, B., & Goodman, J. 1993, *ApJ*, 413, L7 (SPG)
Teegarden, B. J., et al. 1993, in *AIP Conf. Proc.* 280, *Compton Gamma-Ray Observatory*, ed. M. Friedlander, N. Gehrels, & D. Macomb (New York: AIP), 860
Witt, H. J. 1990, *A&A*, 236, 311
———. 1993, *ApJ*, 403, 530